Mechanistic Insights into the Demethylation of Lignin-Derived Structures using Protic Ionic Liquids: A DFT Study

*Dhirendra Kumar Mishra[1,2], Kenneth L. Sale[1,3], Blake A. Simmons[1,4], and Hemant Choudhary[1,2]**

[1] Deconstruction Division, Joint BioEnergy Institute, 5885 Hollis Street, Emeryville, California 94608, United States
[2] Bioresource and Environmental Security Department, Sandia National Laboratories, 7011 East Avenue, Livermore, California 94551, United States
[3] Department of Computational Biology and Biophysics, Sandia National Laboratories, 7011 East Avenue, Livermore, California 94551, United States
[4] Biological Systems and Engineering Division, Lawrence Berkeley National Laboratory, 1 Cyclotron Road, Berkeley, California 94720, United States

***Email:** hchoudhary@lbl.gov; hchoudh@sandia.gov

ORCID Details:
DKM: https://orcid.org/0000-0002-5730-7834
KLS: https://orcid.org/0000-0002-4269-8940
BAS: https://orcid.org/0000-0002-1332-1810
HC: https://orcid.org/0000-0003-2847-3080

Abstract

Lignin valorization is hindered by the resilience of its methoxy groups to cleavage, necessitating efficient demethylation strategies. Herein, we employ density functional theory (DFT) to elucidate the intricate mechanistic pathways of demethylation in lignin model compounds, specifically guaiacol and syringol, employing protic ionic liquids (PILs) as both solvents and catalysts. A comprehensive COnductor like Screening MOdel for Real Solvents (COSMO-RS) analysis identified monoethanolammonium acetate ([MEOA][Ace]) as the optimum solvent for demethylation due to its superior solvation properties resulting from strong hydrogen-bonding capabilities. By integrating implicit and explicit solvation models, we elucidated the demethylation reaction pathways and energy barriers, highlighting that an acid-catalyzed hydrolytic mechanism directs the demethylation process. Critical electronic structure investigations, including HOMO–LUMO gap evaluations, charge distribution, and electrostatic potential mapping, revealed the role of PILs in stabilizing transition states and intermediates. These findings provide atomic-level insights into reaction dynamics and underscore the potential of tuning acid concentration in PILs to improve demethylation kinetics, facilitating a rational framework for next-generation biomass conversion technologies.

Keywords: Lignin, Density Functional Theory, COSMO-RS, Protic ionic liquids, HOMO-LUMO

Introduction

Lignin is a critical component of lignocellulosic biomass and one of the most abundant renewable polymers on Earth, accounting for up to 30% of the organic carbon in the biosphere [1]. Its complex three-dimensional architecture, built from phenylpropanoid units connected by various ether (e.g., β-O-4, α-O-4, 4-O-5) and carbon–carbon (e.g., β–β, β–5, 5–5) linkages, is largely influenced by its high methoxy content [2,3]. While these methoxy groups contribute to lignin's structural integrity, they also contribute to its chemical inertness and recalcitrance, limiting its applications to low-value uses such as heat and electricity generation [4–8]. However, the relationship between lignin reactivity and methoxy group concentration is complex, since these groups can both augment structural stability via steric and electronic influences and act as reactive sites for certain chemical transformations under suitable catalytic conditions. Demethylation, which converts methoxy groups into reactive phenolic hydroxyl groups, offers a transformative approach to enhancing lignin's reactivity and expanding its applications in advanced materials, bio-based polymers, adhesives, and other high-value chemicals (Scheme 1) [9,10]. The consequent increase in phenolic hydroxyl groups improves properties including metal-binding and antioxidant activity, hence increasing lignin's potential in various applications [11,12]. These benefits highlight the need of developing effective and selective demethylation techniques as a key strategy for sustainable lignin use and the advancement of green chemistry [13–15]. Traditional demethylation approaches have predominantly relied on harsh conditions including concentrated mineral acids (HBr, HI) or toxic reagents like iodocyclohexane. However, these methods suffer from significant drawbacks including high cost, long-term viability concerns, and side reactions like condensation that can reduce product quality [16–18]. On the other hand, biological methods using P450 enzymes exemplify the precision of biocatalysis for lignin demethylation, however, their limited stability, high cofactor costs, narrow substrate scope, low reaction rates, and complex process requirements render them less effective than ionic liquid or chemical catalyst methods for industrial lignin valorization. Ionic liquids combine solvent and catalytic functions in a single medium, offering faster, broader, and more cost-efficient demethylation routes under scalable conditions [19–21].

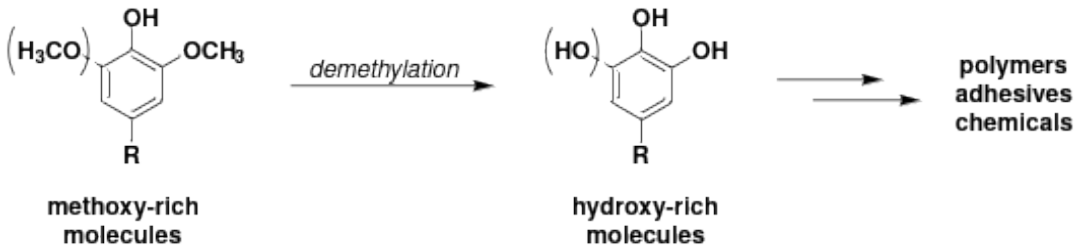

Scheme 1. Schematic representation of demethylation of lignin-derived methoxy-rich molecules (e.g., guaiacol or syringol) into hydroxy-rich molecules (e.g., catechol or pyrogallol).

Comprehensive mechanistic knowledge of the demethylation process is essential due to lignin's structural heterogeneity and the complexity of itschemical reactions and reaction pathways.

Traditional experimental methods have struggled to detect transient intermediates and subtle electronic effects essential to the reaction [22–24]. Density Functional Theory (DFT) has become an indispensable computational tool for modeling chemical reaction mechanisms, enabling precise calculations of reaction pathways, identification of transient intermediates, and analysis of electronic effects governing catalytic processes [25,26]. By incorporating solvent effects and investigating multiple reaction pathways, DFT allows the prediction of activation energies, construction of potential energy surfaces, and identification of key transition states and intermediates [25,27–30]. However, due to lignin's large size and structural complexity, DFT simulations require significant computational resources [31–33]. To address this challenge, model compounds such as guaiacol and syringol are commonly used, as they capture the fundamental aromatic components and reactivity patterns of lignin, while limiting compute times. [34–36]

As alternative solvents for biomass processing, the search for greener and more efficient reaction media has focused on ionic liquids (ILs) [37–39]. Among them, protic ILs (PILs) have attracted attention because of their dual role as solvents and catalysts, along with their thermal stability, low vapor pressure, and remarkable solvation capacity [40–42]. Under mild conditions, PILs are particularly appealing for processing recalcitrant biopolymers like lignin due to their simple synthesis, cost-effectiveness, improved biodegradability, and lower toxicity compared to conventional imidazolium-based ILs. Their ability to both dissolve lignin and catalyze specific chemical transformations, such as demethylation, makes them promising candidates for sustainable, large-scale biomass conversion [43–45].

In this work, we investigate alkanolamine-based PILs (Figure 1), with initial studies focusing on monoethanolammonium acetate ([MEOA][Ace], a PIL with a strong potential for lignin processing. By partially transferring protons between cations and anions, [MEOA][Ace] maintains a balance between reducing excessive acidity, preserving ionic character, and preventing destabilizing full ionization. This balance enables its nucleophilic and proton-donating properties to effectively cleave methoxy groups from lignin-derived substrates while minimizing side reactions such as condensation and over-degradation [46,47]. Additionally, the solvent environment provided by [MEOA][Ace] may stabilize key chemical intermediates and transition states, thereby lowering the activation barrier for demethylation. To fully evaluate its catalytic role and interactions with lignin model compounds, we integrate [MEOA][Ace] into a DFT computational framework, optimizing the reaction pathway for maximum selectivity and efficiency.

The goal of this work was to elucidate the mechanistic pathway for the demethylation of lignin-derived compounds in the presence of [MEOA][Ace] using advanced DFT calculations. Simulations were performed using guaiacol (2-methoxyphenol) and syringol (2,6-dimethoxyphenol) as model compounds, chosen for their structural simplicity and relevance as primary byproducts of lignin depolymerization. Guaiacol and syringol represent the guaiacyl (G) and syringyl (S) units of lignin, respectively, which are fundamental building blocks of this

complex biopolymer. Their selection allows a focused investigation of the chemical behavior of lignin or lignin-derived monomers during demethylation reactions, while providing insights into the distinct reactivity associated with G and S units. We aim to identify key reaction intermediates and transition states, estimate activation energies, and determine the rate-limiting steps governing the reaction kinetics. To further understand factors influencing reactivity, detailed electronic structure studies including assessments of the HOMO–LUMO energy gap and Mulliken charge distribution were performed, which offered insight that helped rationalize [MEOA][Ace] as an effective catalytic system for lignin valorization.

This work intended to pave the way for more effective and economically viable biomass conversion technologies by addressing lignin recalcitrance through targeted demethylation and leveraging the unique properties of PILs. The findings of this work are expected to inspire further research, supporting the development of new catalytic systems and reaction strategies tailored to the specific challenges of lignin valorization, thereby contributing to a more sustainable biorefineries and chemical industry.

Computational details

COSMO-RS calculations

The Conductor-like Screening Model for Real Solvents (COSMO-RS) calculations were conducted in accordance with numerous simulation steps. Initially, the Amsterdam Density Functional (ADF) application was used to generate the geometries of all the molecules under investigation, including guaiacol, syringol, and acceptor and donor molecules that are associated with PILs [48]. Molecular geometries were optimized at the BP86 level of theory and the def2-TZVP basis set using the Turbomole package [49]. Frequency calculations were then performed to confirm that the optimized structures represent true energy minima on the potential energy surface. In other words, the absence of imaginary vibrational frequencies verifies that the geometries are stable, and these calculations also provide thermodynamic corrections to the computed energies. Following the successful geometry optimization, the COSMO file was generated using the BP86/def2-TZVP/DGA1 level of theory and basis set. The electron density can be spatially adjusted to the extent that is appropriate for the specific molecular environment through the combination of def2-TZVP and DGA1 basis sets [50–53]. The COSMO files were then used as input to the COSMOtherm package (version 23.0.1, COSMOlogic, Leverkusen, Germany). Utilizing the BP_TZVP_19 parametrization, the logarithmic activity coefficients (ln(γ)) of mixtures were computed.

Density functional theory (DFT) calculations

The density functional theory (DFT) was used to conduct quantum chemical calculations. The BP86 functional and the split valence basis set def2-TZVP were implemented in the ORCA 5.0.4 package [54]. In order to investigate the demethylation pathways of guaiacol and syringol, the structural optimization of the reactants, products, intermediates, and transition states (TS) was conducted at the BP86/def2-TZVP level of theory [55]. The stationary sites were identified through

the potential energy surface (PES) scan. The frequency calculations corroborated the nature of each stationary point and their vibrational modes, which were then analyzed using the ADF visualization program[48]. The transition state (TS), also referred to as the first-order saddle point, has a single imaginary frequency that corresponds to its optimized electronic structure, while the stationary point at minima has all real frequencies. Additionally, it was ensured that each TS connected its reactions and products via a minimum energy path (MEP) on the potential energy surface by conducting intrinsic reaction coordinate (IRC) calculations at the same level of theory [56]. Subsequently, the energy accuracy was improved by employing the optimized geometries for single point energy calculations with a more precise basis set def2-TZVP. The BP86 method provides a balanced approach that is appropriate for the study of the mechanisms and kinetics of gas-phase reactions, with sufficient accuracy and moderate computational effort at the def2-TZVP basis set [52]. The chemical reactivity of the guaiacol, syringol and PIL–water-model compound complex systems was investigated using frontier molecular orbital (FMO) analysis. The AMSsuite program was employed to visualize the isosurface map of MEP, as indicated by the ORCA outputs [48]. NCI analysis was conducted using the Multiwfn 3.8 program [57]. The VMD 1.9.3 program was used to generate all NCI maps [58].

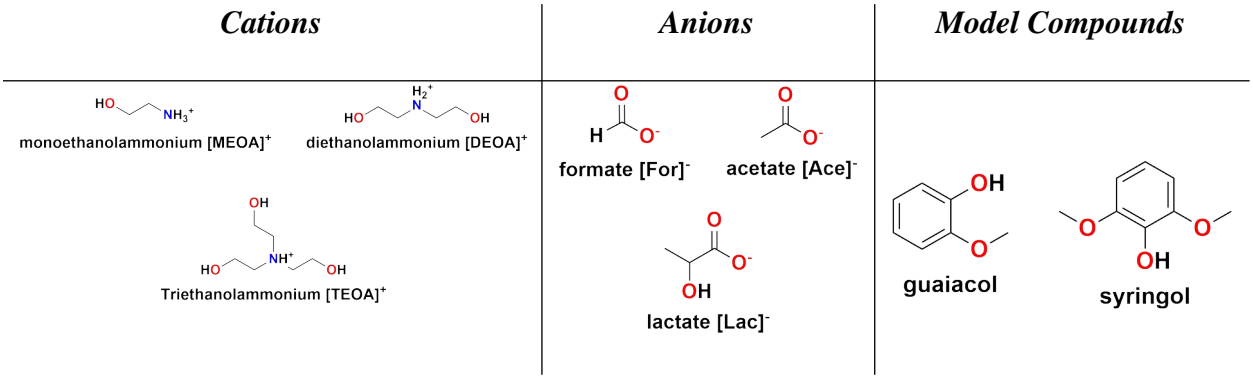

Figure 1. Molecular structures of the compounds used in the study.

Results and discussion

COSMO-RS calculations

In this investigation, nine PILs were studied, all originating from alkanolamine-based cations combined with carboxylate anions. The PILs included monoethanolammonium formate [MEOA][For], monoethanolammonium acetate [MEOA][Ace], monoethanolammonium lactate [MEOA][Lac], diethanolammonium formate [DEOA][For], diethanolammonium acetate [DEOA][Ace], diethanolammonium lactate [DEOA][Lac], triethanolammonium formate [TEOA][For], triethanolammonium acetate [TEOA][Ace], and triethanolammonium lactate [TEOA][Lac]. The chosen PILs provide a unique combination of solvent and catalyst properties, making them highly effective for dissolving lignin and catalyzing the selective cleavage of methoxy groups through nucleophilic substitution. Furthermore, their capacity to function under gentle and eco-friendly

conditions, along with adjustable acidity/basicity and the potential for reuse, significantly boosts their appropriateness for sustainable lignin valorization methods [59].

Initially, we employed the COSMO-RS model to evaluate various PILs for their capacity to dissolve guaiacol and syringol. The model's predictions indicated that [MEOA][Ace] exhibited the highest potential for effectively dissolving these compounds. After successful screening of a set of PILs for lignin derived structures, we predicted the logarithmic activity coefficient (ln(γ)) for the model compounds. The significance of ln(γ) values lies in their direct correlation to the molecular-level interactions and system non-ideality. Lower ln(γ) values (negative logarithmic values) indicate stronger attractive forces between solute and solvent molecules, suggesting favorable dissolution and mixing processes. Conversely, higher ln(γ) values (positive logarithmic values) signify weaker interactions and potential phase separation tendencies [60,61]. The magnitude of these values provides quantitative insights into the degree of molecular affinity between the solute and PILs. When ln(γ) approaches unity (logarithmic value approaches zero), the solution behavior approaches ideality, indicating balanced interactions between solute-solute and solute-solvent molecules, and the corresponding ln(γ) values then serve as a solubility indicator in solvents, with negative values denoting solubility and positive values indicating insolubility [62]. These values thus serve as crucial parameters for assessing solvent capacity and selectivity in separation processes, particularly in the context of lignin-derived compound extraction and purification [32,33,63,64]. The electrostatic iso-surfaces relevant to the studied systems are provided in the Supporting Information (Figure S1). These iso-surfaces were derived from "*.cosmo*" files generated and were employed in the analysis of solubility properties.

The ln(γ) of syringol and guaiacol in alkanolamine-based PIL systems demonstrate significant variations that can be attributed to the specific molecular interactions between the solutes and the PIL. In systems where amines function as cations and organic acids serve as anions, the observed activity coefficients provide crucial insights into the solubility behavior and molecular-level interactions (Figure 2). Figure 2 demonstrates that guaiacol had negative ln(γ) values across all tested alkanolamine-based solvents, while syringol consistently had positive ln(γ) values. This phenomenon can be attributed to multiple factors within the molecular framework. The presence of the hydroxy group in $[MEOA]^+$ facilitates hydrogen bonding with the methoxy and hydroxy groups present in both syringol and guaiacol. Additionally, the $[Ace]^-$ anion contributes to the formation of a hydrogen bond network, creating a favorable environment for these lignin-derived compounds. Another factor may be structural differences between guaiacol and syringol—specifically, syringol contains an extra methoxy group on the aromatic ring. Although both guaiacol and syringol can engage in hydrogen bonding, the additional methoxy group in syringol may introduce greater steric hindrance and alter the electron distribution around the phenolic hydroxyl group. As a result, syringol's ability to form favorable hydrogen bonds with ammonium-based PILs is reduced compared to guaiacol (Figure S4).

The trend in activity coefficients across different PILs correlates strongly with the hydrogen bond donor and acceptor capabilities of the constituent ions. Systems with positive ln(γ) values typically demonstrate weaker interactions between the solute and PIL components, often due to steric hindrance or reduced hydrogen bonding capability [65]. This is particularly evident in PILs with longer amine chain length and size of carbon chain in acids, where the accessibility of interaction sites becomes limited [66]. The lower ln(γ) values observed for both syringol and guaiacol in [MEOA][Ace] compared to other PIL systems indicate enhanced solubility and stronger favorable interactions. The structural compatibility between $[MEOA]^+$ hydroxyl group and the phenolic structures of syringol and guaiacol forms an efficient hydrogen bonding network. The relatively small size of both the $[MEOA]^+$ cation and $[Ace]^-$ anion minimizes steric effects that could hinder solute-solvent interactions. Furthermore, the moderate basicity of $[MEOA]^+$ combined with the $[Ace]^-$ anion's hydrogen bond acceptor characteristics creates an ideal environment for stabilizing these aromatic compounds [67,68]. The lower positive ln(γ) values for syringol in [MEOA][Ace] compared to other PILs indicate a potential enhancement in solute-solvent interactions or a decrease in steric hindrance. This observation was a key factor in selecting [MEOA][Ace] to study the reaction pathway, as it provides a more favorable environment for investigating syringol's behavior despite its limited solubility.

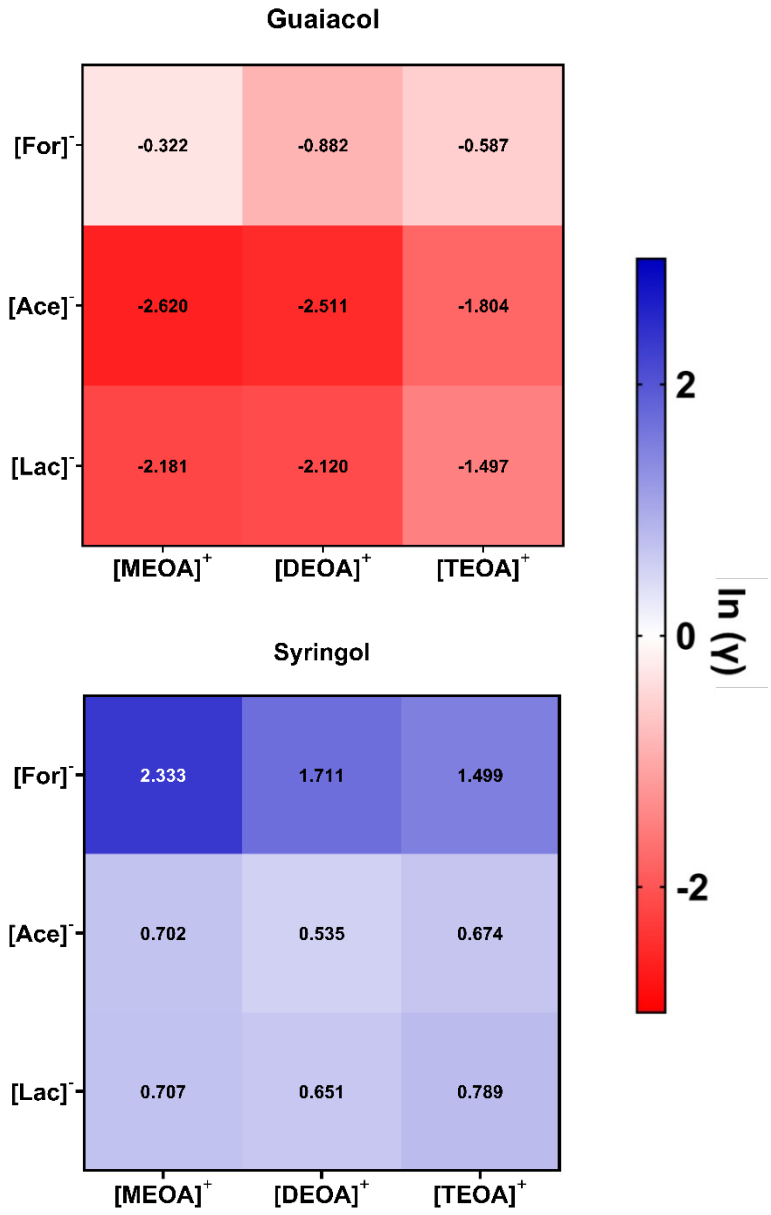

Figure 2. COSMO-RS predicted heatmap of ln(γ) for guaiacol and syringol with different combinations of alkanolamine based PILs.

The underlying chemistry governing these interactions was further elucidated through examination of the specific molecular structures. The phenolic hydroxyl groups in both syringol and guaiacol act as hydrogen bond donors, while their methoxy groups serve as weak hydrogen bond acceptors. In [MEOA][Ace], the $[Ace]^-$ anion's carboxylate group provides two oxygen atoms capable of accepting hydrogen bonds, while the $[MEOA]^+$ offers both hydrogen bond donor (NH_2 and OH groups) and acceptor (OH group) sites. This complementary arrangement creates a hydrogen

bonding network that effectively encapsulates the solute molecules (Figure S2). The π-electron system of the aromatic rings in syringol and guaiacol can also participate in cation-π interactions with the nitrogen atom of $[MEOA]^+$, further stabilizing the system [69]. The solubility behavior predicted by ln(γ) values of guaiacol and syringol in PILs was compared with their respective ΔpK_a values to understand the fundamental interaction mechanisms. Here, ΔpKa is defined as the difference between the pKa values of the carboxylic acid and the phenolic compound. A high ΔpKa signifies a marked difference in their acid strengths, which promotes proton transfer and the establishment of strong intermolecular interactions such as ion pairing and robust hydrogen bonding. Conversely, a low ΔpKa indicates that the acid and the phenol possess similar acidities, leading to limited proton exchange. The ΔpK_a values were calculated between the model compounds and the constituent acids (formic acid: 3.75, acetic acid: 4.76, and lactic acid: 3.86). For guaiacol (pK_a = 9.98), the ΔpK_a values with acids ranged from 5.22 to 6.23, while syringol (pK_a = 9.37) showed relatively lower values ranging from 4.61 to 5.62. Interestingly, the ln(γ) values demonstrated that systems with moderate ΔpK_a values exhibited enhanced solubility, particularly evident in acetic acid-based PILs (ΔpK_a = 5.22 for guaiacol and 4.61 for syringol) as presented below in Figure 3.

The solubility trends revealed a distinct pattern where the acid component plays a more decisive role compared to the amine group. This is evidenced by the consistent grouping of ln(γ) values across different amine bases while showing marked variations among different acids. For guaiacol, despite formic acid having the highest ΔpK_a (6.23), acetic acid systems demonstrated superior predicted solubility by ln(γ) values, suggesting that optimal proton transfer capability rather than maximum ΔpK_a values governs the dissolution process [70]. This observation is further supported by the hydrogen bonding distances observed in the molecular structures, where acetic acid systems maintain favorable interaction distances of 1.85 Å, facilitating efficient solvation networks. Despite acetic acid being a weaker acid (higher pKa) than formic or lactic acid, its reaction with $[MEOA]^+$ to produce a PIL facilitates strong hydrogen bonding with guaiacol. The structural representations indicate short O–H···O bond distances (~1.8 Å), suggesting a stable hydrogen-bond network, despite the overall acid–base interaction being less pronounced compared to stronger acids. The PIL environment enhances the interactions between weaker acids and phenols, promoting effective proton sharing and improving the incorporation of guaiacol into the solvent phase [71]. The moderate interaction between $[Ace]^-$ and guaiacol forms a flexible and dynamic solvation environment that facilitates the dispersion of guaiacol molecules. In contrast, the stronger binding observed with $[For]^-$ or $[Lac]^-$ leads to a more rigid and overly stabilized solvation shell, which restricts molecular mobility and ultimately diminishes overall solubility. The ΔpKa values (5.22 for guaiacol and 4.61 for syringol) and ln(γ) data suggest that $[Ace]^-$-based PILs can effectively promote demethylation by making intermediates more soluble and stable. When ΔpKa values are high, like 6.23 for guaiacol-formic acid, they mean that there is strong proton transfer and hydrogen bonding (O-H distance = 1.82 Å). This stabilizes intermediates and lowers

demethylation barriers, but it may change how well the PILs dissolve, as shown by positive ln(γ) values for formic acid-based PILs in case of syringol. $[Ace]^-$-based PILs with lower ΔpKa values, like 4.61 for syringol-acetic acid, have less proton transfer but better solubility as shown by negative ln(γ) values.

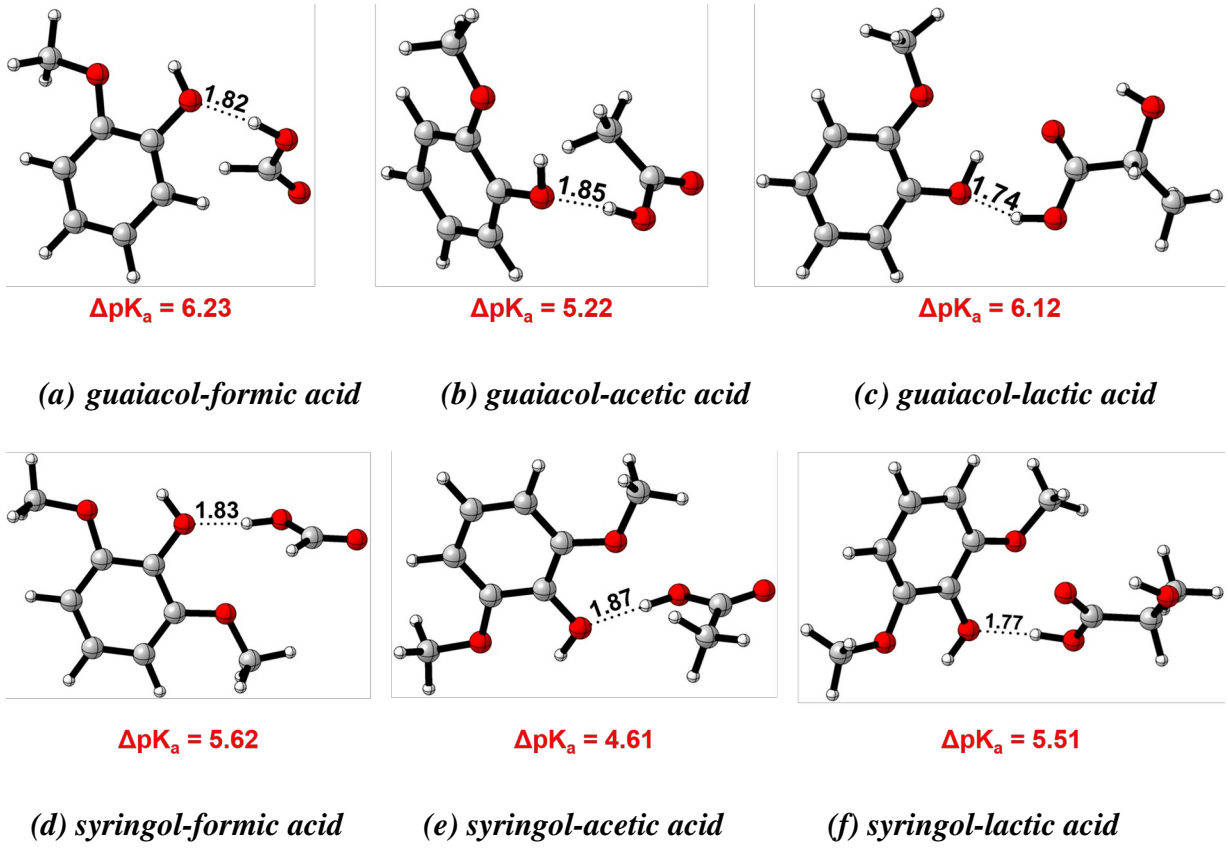

Figure 3. Optimized structures of model compounds with acids, for guaiacol (3a-c) and syringol (3d-f). The values in red correspond to the ΔpK_a value of the related structure. The distances in Å are consistent with H-bond formation.

The similarity in amine-based trends across both solutes (Figure S3), contrasting with the distinct acid-dependent variations, indicates that while the amine component contributes to the overall PIL properties, the acid component predominantly determines the solubility behavior. Guaiacol, with a simpler structure and weaker hydrogen bonding (smaller ΔpKa shifts), displays negative ln(γ) values, reflecting favorable solute-solvent interactions and enhanced solubility. The interactions between the complex systems demonstrate that the structure of amines influences the strength of hydrogen bonding (Figure S3). Monoethanolamine forms stronger hydrogen bonds with shorter bond distances (1.70 and 1.87 Å), which will be helpful for demethylation. Triethanolamine, on the other hand, has weaker interactions because its bonds are farther apart (3.11 Å). The molecular van der Waals (vdW) volume of amines correlates strongly with their ability to interact with guaiacol

and syringol. It was clearly seen that as the bulkiness of the amines increases from monoethanolamine to triethanolamine, its ability to interact effectively with other species, such as guaiacol or syringol, diminishes due to steric hindrance (Table S1). Larger cations tend to have reduced charge density because their positive charge is distributed over a larger volume. Mixing systems with moderate ΔpKa values and monoethanolamine works best for finding a balance between how well they dissolve and react in demethylation processes. Syringol forms weaker bond interactions with amines, and also exhibits positive ln(γ) values in ionic systems, indicating unfavorable solute-solvent interactions and reduced solubility (Figure S3). This is likely due to the steric hindrance and electronic effects of its bulky methoxy groups, which limit effective solvation despite strong hydrogen bonding. The steric effects of model compounds were verified by performing Non-Covalent Interaction (NCI) analysis (Figure S4). The NCI plots based on the reduced density gradient (RDG) provide critical insights into the solubility behavior of syringol and guaiacol. These plots visually highlight regions of attractive and repulsive interactions within the molecular systems. For syringol, the NCI analysis reveals significant steric hindrance due to its bulky methoxy groups, as indicated by pronounced spikes in the RDG plot corresponding to repulsive interactions. These steric effects limit effective solvation, contributing to syringol's reduced solubility despite its strong hydrogen bonding capabilities. In contrast, guaiacol exhibits fewer steric repulsion regions in its NCI plot, reflecting a simpler molecular structure that facilitates better solute-solvent integration. The RDG troughs associated with guaiacol indicate favorable interactions, aligning with its negative ln(γ) values and enhanced solubility. These results highlight the interplay between molecular structure, localized stabilization, and global solvation thermodynamics in determining solubility behavior. The findings regarding acid and base pairs indicate that the solubility of lignin model compounds in protic ionic liquids is influenced by a collaborative equilibrium between the properties of anions and cations: the acetate anion mainly dictates solvation strength by its ability to accept hydrogen bonds from phenolic OH groups, whereas the size and hydrogen-bond donating capacity of the ammonium cation adjust steric accessibility and acid–base interactions in the initial solvation shell, resulting in optimal dissolution only when both elements are effectively aligned.

Reaction pathway for demethylation of guaiacol and syringol in presence of [MEOA][Ace] using CPCM implicit solvation model

The conductor-like polarizable continuum model (CPCM) is a computational technique employed to represent the solvent as a polarizable continuum instead of discrete molecules in which the solute molecule is embedded into a cavity surrounded by a dielectric continuum of permittivity ε. This method markedly decreases computing costs relative to explicit solvent modeling while effectively capturing essential electrostatic interactions between solute and solvent [72]. However, [DEOA][Ace] demonstrates improved solubility for syringol compared to [MEOA][Ace] (Figure 2), the selection of [MEOA][Ace] for both guaiacol and syringol reflects a methodologically

rigorous approach. This decision prioritizes systematic comparability over marginal solubility improvements, as the difference in ln(γ) for syringol between the solvents is negligible relative to the analytical benefits. Maintaining uniform reaction conditions enables robust evaluation of electronic effects, steric constraints, and reaction energetics across both lignin model compounds. Such consistency provides fundamental mechanistic insights into demethylation processes that would be obscured by solvent-dependent variables. The ln(γ) values revealed superior solubility characteristics of [MEOA][Ace] for lignin model compounds, particularly evident from the significantly negative ln(γ) values for guaiacol (-2.5) and relatively moderate positive values for syringol (0.5) (Figure 2). This favorable solubility behavior prompted the investigation of demethylation mechanisms in [MEOA][Ace] using implicit solvation calculations, where water serves as an explicit proton donor in the reaction pathway. The implicit solvation model treats the solvent as a continuous dielectric medium surrounding the solute molecules, accounting for electrostatic and non-electrostatic interactions through a polarizable continuum model, while maintaining explicit representation of specific solvent molecules directly involved in the reaction mechanism. For guaiacol, the demethylation proceeds through a stepwise process with an initial energy barrier of 41.19 kcal/mol to form the first intermediate, followed by a transition state at 66.97 kcal/mol. The lower energy requirements correlate well with the negative ln(γ) values, suggesting that the favorable solvation environment provided by [MEOA][Ace] facilitates the formation and stabilization of reaction intermediates. The final product stability (-5.32 kcal/mol) further supports the thermodynamically favored guaiacol demethylation in [MEOA][Ace] (Figure 4a) [73,74].

In contrast, syringol follows a more energetically demanding pathway. While the initial intermediate formation requires less energy (35.49 kcal/mol), attributed to enhanced carbocation stabilization by the additional methoxy group, the system encounters a substantially higher transition state barrier (75.21 kcal/mol). This elevated energy requirement aligns with the less favorable solubility behavior observed in ln(γ) measurements, where positive ln(γ) values indicate suboptimal solvation. The final product demonstrates marginal thermodynamic favorability (-0.22 kcal/mol), consistent with the observed solubility trends. The correlation between reaction energetics and solubility behavior in [MEOA][Ace] provides mechanistic insights into the role of the solvent environment. The moderate ΔpKa value (5.22) of [MEOA][Ace] appears to form an optimal balance for guaiacol interactions, while the higher transition state barrier for syringol suggests that structural factors significantly influence both reaction progression and solubility [73]. The implicit solvation model with explicit water as a proton donor effectively captures these differences, demonstrating how solvent-solute interactions manifest in both thermodynamic and kinetic aspects of demethylation [75].

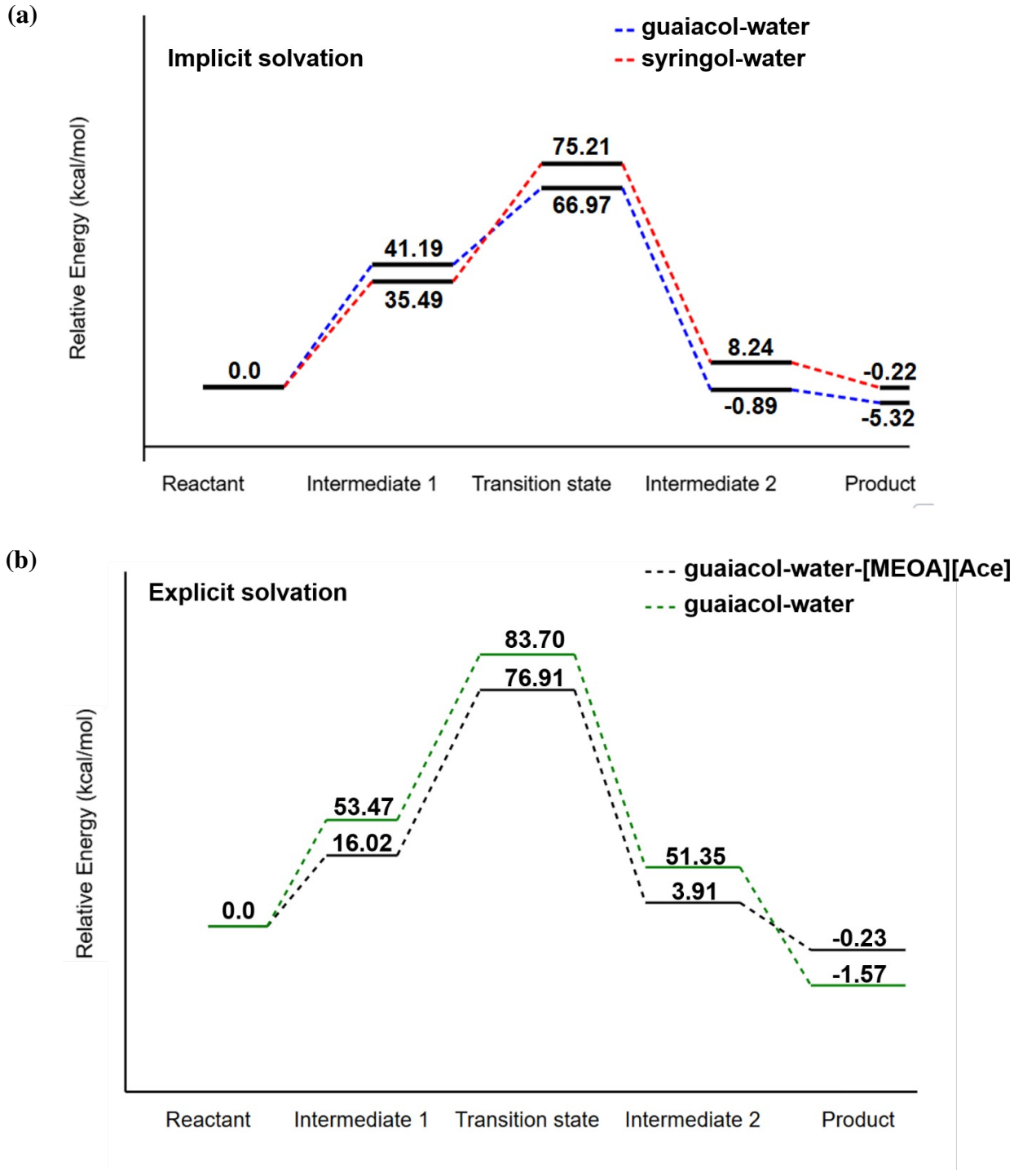

Figure 4. Relative energy curve for **(a)** guaiacol-water and syringol-water system using implicit solvation model, and **(b)** guaiacol-water-[MEOA][Ace] and guaiacol-water system using explicit solvation model. All energies are in kcal/mol.

The results discussed above through Figure 4(a) demonstrated that guaiacol exhibited a lower activation energy barrier compared to syringol, making it a more efficient system for the reaction.

Building on these findings, we extended our analysis by incorporating explicit solvation models to further explore the role of explicit interactions between guaiacol, water, and the PIL ([MEOA][Ace]). This approach aims to validate and deepen our understanding of how the PIL influences the reaction mechanism and its energy profile.

The explicit solvation model calculations were performed for two systems: guaiacol-water and guaiacol-water-[MEOA][Ace]. The energy profile depicted in Figure 4(b) provides a comparative analysis of these systems. For the guaiacol-water system (green line), the activation energy barrier for the transition state is 76.91 kcal/mol. In contrast, when [MEOA][Ace] is introduced into the system (black line), the activation energy barrier decreases significantly to 53.47 kcal/mol. This substantial reduction highlights the catalytic effect of the PIL in facilitating the reaction by lowering the energy required to reach the transition state. The plot also reveals differences in intermediate stabilization and product formation between the two systems. For Intermediate 1, the relative energy is notably lower in the guaiacol-water-[MEOA][Ace] system compared to guaiacol-water alone. Similarly, at Intermediate 2 and product stages, the PIL system consistently demonstrates lower relative energies (-0.23 kcal/mol for products) compared to water alone (-1.57 kcal/mol). These observations suggest that [MEOA][Ace] not only reduces the activation energy but also stabilizes intermediates and products more effectively than water.

The inclusion of explicit solvation effects was crucial for verifying and quantifying the influence of [MEOA][Ace] on this reaction. While implicit solvation models provide valuable insights into general trends, explicit solvation captures specific interactions between solvent molecules and reactants that contribute to energy stabilization or destabilization along the reaction pathway. The explicit calculations confirm that [MEOA][Ace] enhances reaction efficiency by lowering activation barriers and stabilizing key intermediates, thereby demonstrating its potential as a superior solvent system compared to water alone.

Reaction pathway for demethylation of guaiacol in the presence of [MEOA][Ace]

To gain a deeper insight into the specifics of the guaiacol-water and PIL reaction system, we conducted a detailed calculation of the reaction pathway using an explicit solvation model to clarify the electronic and structural aspects of the reaction mechanism[76]. We initiated our investigation with a single molecule of guaiacol and syringol, which represents the fundamental G and S unit of the lignin complex. This is a well-established protocol in DFT, in which simplified models are employed to establish fundamental principles before progressing to more complicated investigations. Simultaneously, we utilized a minimal explicit solvation approach (one water + one PIL) instead of a comprehensive solvent network, motivated by essential computational constraints and our main research goal of clarifying mechanistic pathways rather than achieving quantitative kinetic replication. In next step, we studied the structural details about the demethylation processes of syringol and guaiacol, focusing on several stages along the reaction coordinate. Though they

show different reactivity profiles, syringol and guaiacol follow similar demethylation routes with water and [MEOA][Ace].

The demethylation mechanisms of guaiacol and syringol in aqueous [MEOA][Ace] systems reveal distinct structural and energetic behaviors influenced by molecular architecture, bond distances, and solvent-substrate interactions. Guaiacol, with its singular methoxy group, exhibits a simpler reaction pathway where initial stabilization arises from hydrogen bonding between its hydroxyl group and water, with the O–H bond measuring 0.96 Å and the hydrogen bond distance being 2.02 Å. The methoxy group aligns effectively with the PIL's cationic moieties, facilitating partial charge transfer between the methoxy oxygen and the PIL's anion. This interaction weakens the C–O bond, elongating it from 1.43 Å in the reactant state to 2.27 Å in the transition state, while simultaneously forming a new bond between the methyl group and the PIL at a distance of 1.48 Å. The transition state is stabilized by cooperative interactions where the PIL's cations electrostatically stabilize the departing methyl group and water molecules stabilize the protonated hydroxyl group through hydrogen bonding. Upon cleavage of the C–O bond, methanol is released as a byproduct, with its hydroxyl group forming a stabilized hydrogen bond at 1.42 Å with water, while the remaining catechol-like product reorients its hydroxyl group toward PIL interactions for further stabilization (Figures 5a-d).

Syringol, on the other hand, presents a more complex reaction pathway due to its dual methoxy groups, which introduce steric constraints and competition for PIL interaction. While its hydroxyl group forms a slightly weaker hydrogen bond with water at 2.09 Å compared to guaiacol's 2.02 Å, the two methoxy groups compete for alignment within the PIL environment. During demethylation, one methoxy group elongates from 1.43 Å in the reactant state to 2.16 Å in the transition state, but steric hindrance from the second methoxy group disrupts optimal orientation with $[MEOA]^+$. This steric interference forces the reacting methoxy group into a skewed orientation, increasing torsional strain and raising the energy required for bond cleavage compared to guaiacol. While the $[Ace]^-$ anion partially stabilizes the transition state through electrostatic interactions, spatial crowding limits full charge delocalization. After demethylation, the remaining methoxy group reorients to minimize steric clash, while methanol stabilizes via hydrogen bonding at a distance of 1.42 Å similar to guaiacol's pathway (Figures 5e-h).

The structural orientations of guaiacol and syringol play critical roles in stabilizing intermediates and transition states during demethylation reactions. Guaiacol benefits from planar alignment of its singular methoxy group with PIL species, allowing linear charge redistribution during bond cleavage and minimizing distortion in the transition state. This alignment ensures efficient stabilization of both the leaving methyl group and the aromatic system concurrently, resulting in lower activation energy requirements. Syringol's dual methoxy groups disrupt planar geometry due to steric repulsion between substituents and PIL cations, forcing one methoxy group into a reactive position while the other adopts a perpendicular orientation to avoid crowding. This

skewed configuration elongates transition-state bonds and introduces electronic imbalance that requires additional energy input for stabilization. Hydrogen bonding networks also influence stabilization dynamics significantly. Guaiacol's hydroxyl group forms stable hydrogen bonds with water or PIL species that anchor its aromatic ring during reaction progression, while syringol's analogous interactions are less efficient due to steric interference from its second methoxy group.

The activation energy disparity between guaiacol and syringol underscores how molecular architecture modulates reaction kinetics in lignin-derived phenolic systems. Guaiacol's simpler structure allows efficient solvent-substrate synergy that reduces energy barriers for demethylation, while syringol's steric bulk introduces spatial conflicts that hinder charge redistribution and increase energetic demands during bond cleavage and intermediate stabilization.

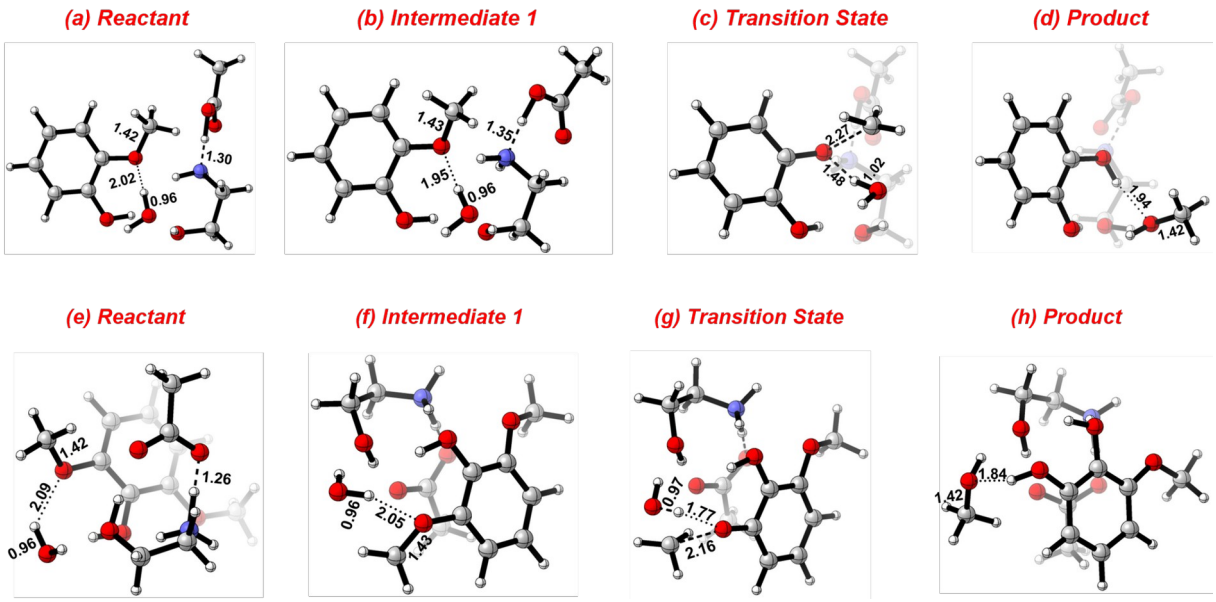

Figure 5. Optimized geometries of different states involved in the demethylation pathway of guaiacol (a-d) and syringol (e-h) in the presence of [MEOA][Ace].

The electronic energy barriers derived from our static DFT optimizations often surpass the associated Gibbs free energy of activation by 10-20 kcal mol^{-1}. However, when entropic and thermal corrections at 298 K are accurately accounted for, these barriers can significantly reduce to the range of 25-35 kcal mol^{-1}, aligning with observable kinetics at room temperature. Moreover, our cluster-continuum model with minimal explicit solvation effectively captures essential hydrogen-bonding interactions. This indicates that employing more advanced explicit-solvent approaches could further lower both the activation barriers and intermediate energies by improving solvent reorganization and entropic stabilization effects.

Building on the earlier steps, it was intriguing to explore the potential of adjusting the acidity of the PIL system by increasing the mole ratio of acetic acid within it. The energy profiles for the hydrolytic demethylation of guaiacol in [MEOA][Ace] unveil complex mechanistic insights

through systematic variation of acetic acid concentration. The computational analysis reveals a significant reduction in the activation energy barrier, dropping from 76.91 kcal/mol (1:1) to 73.5 kcal/mol (1:2) and further decreasing to 71.2 kcal/mol (1:4) (Figure 6). This systematic reduction can be attributed to improved protonation of the methoxy group (-OCH_3) due to greater proton availability and the establishment of more intricate hydrogen bonding networks in the reaction medium [77].

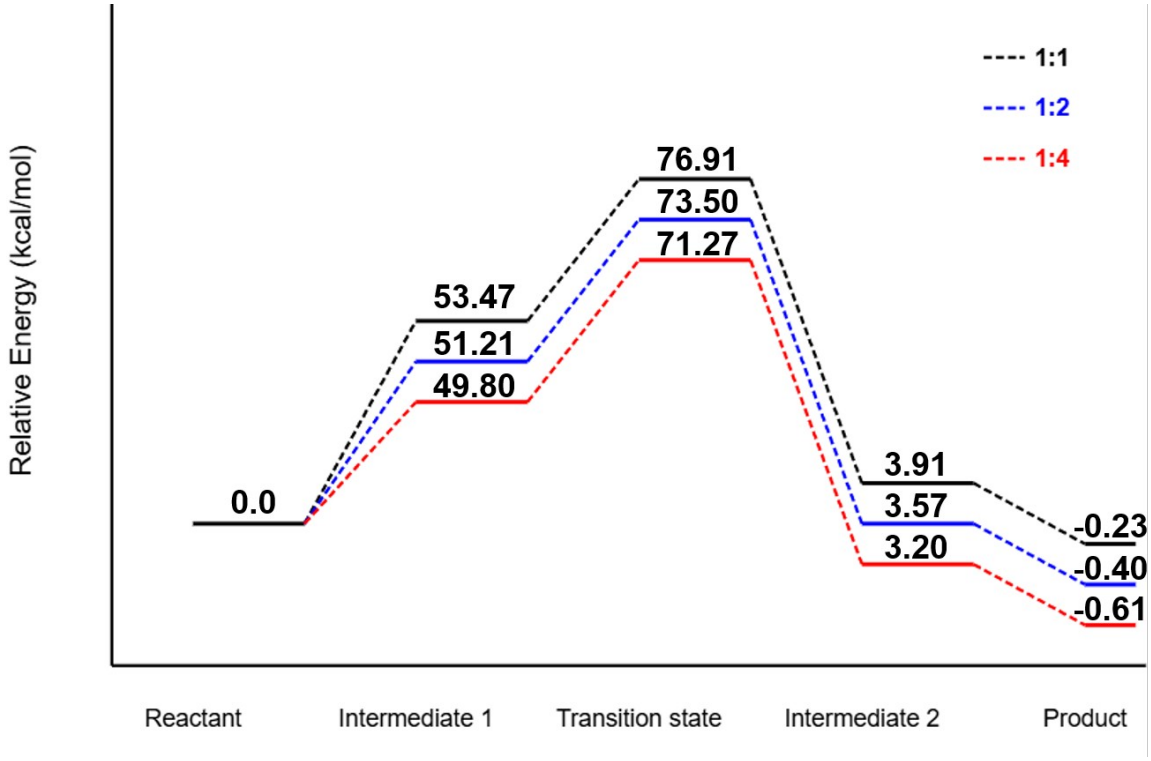

Figure 6. Relative energy profiles for guaiacol demethylation in water-[MEOA][Ace] with varying molar ratios of monoethanolamine and acetic acid (1:1, 1:2, and 1:4). All calculated energies are in kcal/mol.

The function of extra acetic acid molecules within the PIL setting seems to be complex and varied. Initially, homoconjugation amplifies the effective acidity as acetic acid molecules form hydrogen-bonded dimers and oligomers, thereby increasing the system's ability to release protons. Furthermore, these extra acid molecules probably play a role in stabilizing the emerging charge in the transition state via secondary hydrogen bonding interactions. The PIL system, consisting of [MEOA][Ace], promotes this stabilization via collaborative interactions among the ionic species and a heightened presence of acetic acid molecules. The $[Ace]^-$ anions can establish hydrogen bonds with the acetic acid molecules and the protonated methoxy group, thereby fostering a more conducive environment for the demethylation process [78].

An especially significant finding is that the activation barrier exhibits a clear dependence on acid concentration indicated in Figure 6, whereas the energetics of Intermediate 2 and the final product stay fairly stable across the three ratios (3.91 → 3.57 → 3.2 kcal/mol for Intermediate 2 and -0.23 → -0.4 → -0.6 kcal/mol for the product) (Figure 6). This indicates that the concentration of the acid primarily affects the nucleophilic substitution mechanism instead of the final thermodynamic state of the reaction. The slight differences in the energies of the final products suggest that after surpassing the crucial demethylation step, which may involve a transition state akin to SN2, the reaction continues along energetically comparable routes, irrespective of the acid concentration [79].

The first intermediate shows a gradual yet consistent reduction in relative energy (53.47 → 51.2 → 49.8 kcal/mol) as the acid concentration rises as shown in Figure 6. This trend indicates a more effective stabilization of the protonated intermediate species via improved hydrogen bonding networks. The inclusion of extra acetic acid molecules probably establishes a broader proton-relay network, enhancing the transfer of protons to the methoxy oxygen and stabilizing the resulting charged entities. This aligns with the established characteristics of carboxylic acids in PILs, where networks of hydrogen bonding can greatly affect reaction pathways and the stability of intermediates [80].

The energetics of the transition state indicate a concerted mechanism in which proton transfer to the methoxy oxygen happens at the same time as C-O bond cleavage. The diminishing activation barriers as acid concentration rises suggest that more acetic acid molecules could be involved in reducing the reorganization energy necessary for this process. The network of hydrogen bonds formed by the PIL and surplus acetic acid probably assists in aligning the reactants in an advantageous configuration for the reaction, while simultaneously stabilizing the emerging charges in the transition state [81,82]. The noted decrease in activation barrier with higher concentrations of acetic acid indicates that precise adjustments to the acid component in PIL systems may offer a viable strategy for improving reaction kinetics while maintaining the thermodynamic driving force largely unchanged [83]. The favorable energy profile throughout the reaction pathway indicates that PIL systems with higher acetic acid content enhance the efficiency of the demethylation process. The increased acid concentration improves catalytic activity, stabilizes transition states, and lowers energy barriers, making these PILs highly effective as reaction media for lignin transformation.

Frontier molecular orbital and charge transfer analysis

Frontier molecular orbital (FMO) analysis is a powerful method for examining donor–acceptor interactions and the reactivity of molecules. The interactions within a specific system can be categorized into hydrogen-bond interactions, electrostatic interactions, and the orbitals between the highest occupied molecular orbital (HOMO) and the lowest unoccupied molecular orbital (LUMO) species. The HOMO indicates a species' ability to donate electrons, reflecting its nucleophilic nature, whereas the LUMO represents a species' capacity to accept electrons,

highlighting its electrophilic characteristics. The HOMO-LUMO energy gap is a measure of the energy required for the addition or removal of electrons from a molecule [25,62,84].

The HOMO-LUMO visualizations demonstrate characteristic orbital symmetry patterns intrinsic to aromatic systems (Figure 7). In both guaiacol and syringol, the HOMO displays typical π-orbital symmetry with electron density primarily localized on the aromatic ring and oxygen substituents. The nodal planes are oriented perpendicular to the molecular plane, maintaining antisymmetric distribution essential for π-bonding [85]. This arrangement facilitates electron delocalization across the aromatic system, contributing to molecular stability and reactivity patterns. Whereas, the LUMO configurations exhibit antibonding π* character with additional nodal planes, showing more diffuse electron density distributions. The spatial orientation of these orbitals differs significantly from the HOMO, creating distinct pathways for electronic transitions and chemical interactions. This orbital arrangement follows the Woodward-Hoffmann principles, governing electronic transitions and reactivity patterns in these systems [86].

PILs introduced into guaiacol and syringol systems provoke significant electronic structural disruption by modulating the HOMO-LUMO gap, thereby enhancing electron mobility and triggering reorganization of the electron distribution of both molecules. From the molecular orbital diagrams, pure guaiacol had a HOMO-LUMO gap of 4.283 eV while pure syringol had a gap of 4.277 eV (Figure 7). Their electrical characteristics change significantly when these compounds interact with water and [MEOA][Ace]; the HOMO-LUMO gaps drop to 4.209 eV for guaiacol-water-[MEOA][Ace] systems and 4.219 eV for syringol-water-[MEOA][Ace] systems.

In these PIL-containing systems, the redistribution of frontier orbitals is particularly intriguing. Based on orbital visualizations, the HOMO in both guaiacol-water-[MEOA][Ace] and syringol-water-[MEOA][Ace] systems were mostly concentrated on the $[Ace]^-$ ion of the PIL. In parallel, the LUMO remained mostly in the aromatic structures of guaiacol and syringol correspondingly. The interesting donor-acceptor link between the PIL and the aromatic molecules resulted from this spatial gap between HOMO and LUMO.

This electronic reorganization, where the $[Ace]^-$ anion acts as an electron donor (HOMO) and the aromatic rings of guaiacol and syringol act as electron acceptors, allows one to explain the noted decrease in HOMO-LUMO gaps. This configuration raises the reactivity of these systems and possibly helps facilitate electron transport routes. Subtle but important variations in energy spacing between frontier orbitals and polarization of the molecular orbitals result from the interaction between the π-electron system of the aromatic rings and the electrostatic field produced by the ionic environment. The HOMO-LUMO gap suggests guaiacol-water-[MEOA][Ace] (4.209 eV) system is notably more chemically reactive than the syringol-water-[MEOA][Ace] system (4.219 eV). This improved reactivity can be ascribed to the more effective electronic coupling between the $[Ace]^-$ anion and the guaiacol molecule, therefore producing a more favorable energy environment

for electron transfer reactions. In addition to steric hindrance and energy gaps, the additional methoxy group in syringol significantly affects the transition-state energy through both positive mesomeric (+M) and inductive (+I) effects. The +M effect occurs when the lone-pair electrons on the methoxy oxygen delocalize into the aromatic π system, enhancing electron density on all ring carbons and making the ring more electron-rich. This resonance donation depletes electron density from the oxygen, resulting in a greater partial positive charge on the methoxy oxygen in syringol than in guaiacol. Thus, the transition state associated with C–O bond breakage is destabilized due to the increased positive character at the reacting oxygen center, elevating the activation energy. Concurrently, the methoxy substituent's –I effect, attributable to the electronegativity of oxygen, further diminishes electron density through the σ framework, therefore amplifying the electron-deficient character of the methoxy oxygen in the transition state. The integrated electronic modulation elucidates the reduction in HOMO density in syringol (more positive) compared to guaiacol, as demonstrated in our frontier orbital analysis. The diminished HOMO density is associated with decreased nucleophilicity at the reaction site, hence contributing to the increased activation barrier for syringol demethylation [87].

The guaiacol system's decreased energy gap suggests a lesser energy barrier for electronic transitions, thereby maybe increasing reaction speeds and sensitivity to chemical transformations in uses like lignin valorization and biomass conversion. Particularly in lignin depolymerization where guaiacol and syringol act as model chemicals, these electronic perturbations have significant ramifications for biomass processing. A smaller HOMO-LUMO gap enhances chemical reactivity by lowering the energy barrier for electron transitions between these orbitals, facilitating interactions with other molecules. With the guaiacol-based system providing particularly promising reactivity profiles due to its lower energy gap, the enhanced reactivity indicated by the reduced HOMO-LUMO gaps suggests that [MEOA][Ace] may facilitate chemical transformations by creating favorable electronic conditions for reaction paths involving these aromatic systems [88]. These results very well align with DFT-predicted reaction mechanism elucidation in the previous section, where guaiacol demonstrated lower activation energy barriers compared to syringol in the [MEOA][Ace] system.

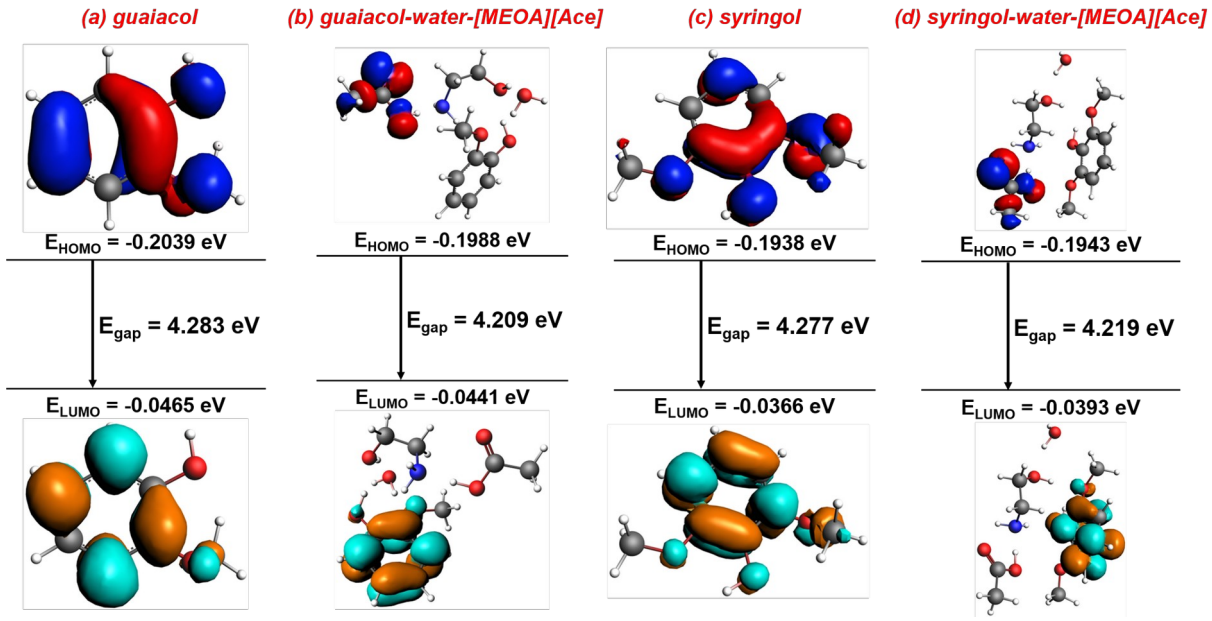

Figure 7. Isosurface of HOMO-LUMO energy gaps between system (a), (b), (c), and (d) all energies are in (eV).

In parallel to HOMO-LUMO analysis of these systems, Mulliken population analysis was performed. Mulliken population analysis is a quantum chemical population analysis approach to calculating the molecular electronic charge distribution of a molecule. It partitions electron density amongst molecule atoms using molecular orbital computations. The fundamental concept calculates each atom's electron population by evaluating atomic orbital contributions and their overlaps with surrounding atoms. Subtracting this computed electron population from the nuclear charge of an atom yields the Mulliken charge. This approach is useful for initial electrical structure investigation despite its basis set requirement [89].

Guaiacol has a modest negative charge (-0.036574) in the guaiacol-water system without PIL, while water has a corresponding positive charge (0.036574). The equal magnitude but opposite signs of these values confirm that guaiacol acts as an electron donor while water serves as the acceptor. This interaction reflects a straightforward redistribution of charge between the two components, driven by guaiacol's ability to donate electrons to water molecules (Table 1). The charge transfer dynamics become more complicated as a result of the involvement of multiple species when water interacts with PILs. As an electron acceptor, water gains electron density with a positive charge transfer value of +0.332123. The role of the $[MEOA]^+$ as an additional electron acceptor is indicated by its positive charge transfer value of +0.276792, whereas the $[Ace]^-$ anion arises as a strong electron donor with a negative charge transfer value of −0.483688.

Significant modifications in charge distribution are observed when the [MEOA][Ace] is introduced to the guaiacol-water system. The negative charge transfer values of the guaiacol molecule

decreases from –0.036574 to -0.022061, suggesting that it has donated a portion of its total electron density to water. The hydrogen bonding forces are influenced, as evidenced by the decrease in the positive charge of the water molecule from +0.036574 to +0.016237. As hydrogen bonding is intrinsically linked to charge transfer processes, where electron density is redistributed between donor and acceptor species. The $[MEOA]^+$ component is most notable for its substantial positive charge (0.831835) acts as a strong electron acceptor, while acetic acid has a negative charge (-0.124314). This suggests that [MEOA][Ace] is actively engaged in the charge transfer processes, with $[MEOA]^+$ serving as an electron acceptor and acetic acid as an electron donor. This results in a redistribution of effective charge transfer network that helps to explain guaiacol's superior solubility and reactivity, as its structure allows for more effective solute-solvent interactions and charge transfer processes, supporting the findings from HOMO-LUMO calculations and Mulliken population analysis.

In the absence of IL, the syringol-water system exhibits a charge separation of comparable magnitude to that of guaiacol, with syringol having a negative charge value (-0.013370) and water having a positive charge value (0.013370). This reduced charge separation may suggest that the basal interactions between syringol and water are less robust than those between guaiacol and water. Notable modifications are observed when [MEOA][Ace] is introduced into the syringol-water system. The negative charge transfer value of the syringol molecule is negligible (-0.000693), indicating that the majority of its excess electron density has been transferred. A reversal in the electronic character of the water molecule is indicated by the development of a negative charge (-0.016392). The [MEOA][Ace] components exhibit a substantial charge separation once more, with [MEOA]+ exhibiting a positive charge transfer value (0.125850) and acetic acid exhibiting a negative charge value (-0.113765).

The role of [MEOA][Ace] appears to be multidimensional. Initially, it functions as a charge transfer mediator, enabling the redistribution of electron density among all system components. The electronic properties of both water and aromatic compounds (guaiacol/syringol) can be altered by the polar environment created by the PIL components (monoethanolamine and acetic acid). Secondly, the natural charge distribution between the lignin model compounds and water is reportedly altered by the presence of PIL, indicating that it alters their interaction patterns. This has the potential to influence properties such as solubility, reactivity, or separation efficacy [90].

The substantial charge on $[MEOA]^+$ in both systems, particularly in the guaiacol-water-PIL system, indicates that it is essential for charge transfer processes. The acetic acid component appears to function as a stabilizing counter-ion, absorbing a negative charge to maintain equilibrium within the system. The charge transfer network established by the [MEOA][Ace] components may be particularly significant for applications that involve the extraction or separation of these aromatic compounds from aqueous solutions. These charge transfer effects illustrate the potential for other PILs to alter the electronic environment of a solution, thereby

facilitating improved control over chemical processes or separations involving these aromatic compounds and are in-line with the HOMO-LUMO analysis. The varying magnitudes of charge transfer between the guaiacol and syringol systems also indicate that PILs may be advantageous for the selective separation or processing of these similar but distinct aromatic compounds.

Table 1. Table for Mulliken Charge analysis guaiacol and syringol systems

system component	water-PIL	guaiacol-water	guaiacol-water-PIL	syringol-water	syringol-water-PIL
guaiacol/ syringol	-	-0.0365(guaiacol)	-0.0220 (guaiacol)	-0.0133 (syringol)	-0.0010 (syringol)
water	+0.3321	+0.0365	+0.0162	+0.0133	-0.0163
$[MEOA]^+$	+0.2767	-	+0.8318	-	+0.1258
$[Ace]^-$	-0.4836	-	-0.1243	-	-0.1137

Anion-dependent energetics of guaiacol demethylation in PILs

It is common to use molecular electrostatic potential (MEP) analysis to predict the active site of chemical reactions[91]. The MEP distribution maps of a variety of PILs are illustrated in Figure 9, where the color scale goes from more negative (red) to more positive (blue) MEP values. Red areas correspond to regions of negative potential, typically associated with electron-rich atoms or groups, such as oxygen in the anions or hydroxyl groups in the cations. These are nucleophilic regions, meaning they are likely to donate electrons in chemical reactions. Blue areas indicate positive potential, often found near electron-deficient atoms and are typically found near hydrogen atoms bonded to electronegative elements like oxygen or nitrogen. As a result, the reaction site is generally identified by the location of the lowest MEP value. While a blue region means that the electrostatic potential is positive, indicating that the part of PIL in this region is more likely to accept electrons, or is more electrophilic relative compared to other regions [91,92]. As shown in Figure 8, in the red MEP region, the maximum ESP values of electrostatic potential are located around hydroxyl groups of $[MEOA]^+$, $[DEOA]^+$, and $[TEOA]^+$.

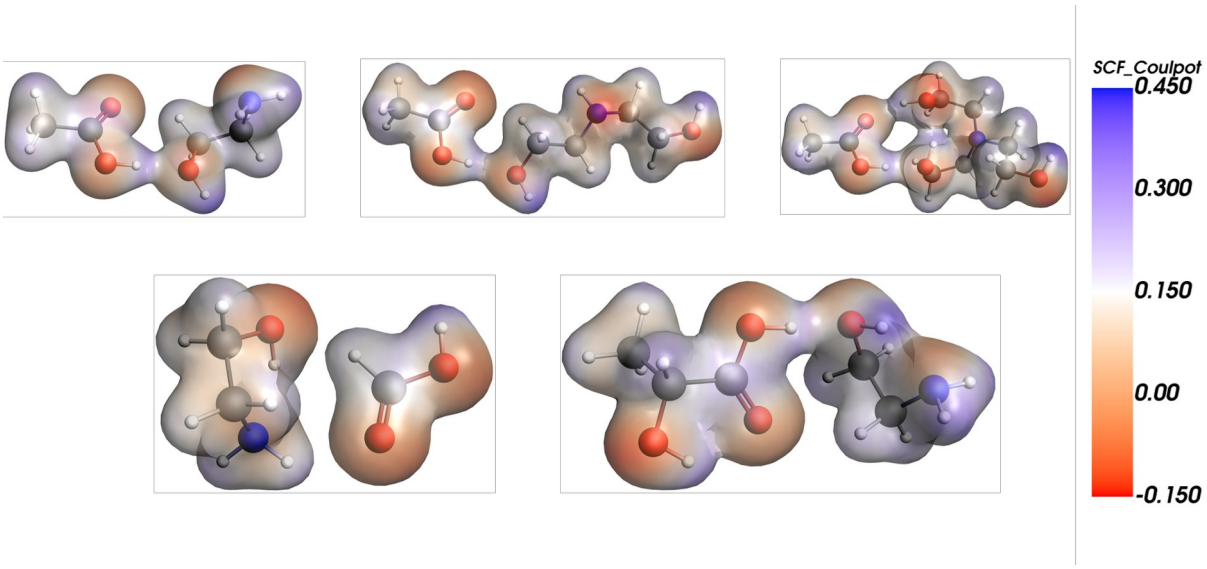

Figure 8. ESP and quantitative distribution of (a) [MEOA][Ace]; (b) [DEOA][Ace]; (c) [TEOA][Ace]; (d) [MEOA][For]; (e) [MEOA][Lac].

The first three structures in the image correspond to PILs with $[Ace]^-$ anions paired with $[MEOA]^+$, $[DEOA]^+$, and $[TEOA]^+$ cations, respectively. As the cation changes from $[DEOA]^+$ to $[TEOA]^+$, the maps show increased nucleophilic activity due to the presence of additional hydroxyl groups in $[DEOA]^+$ and $[TEOA]^+$. These hydroxyl groups contribute more red regions, indicating stronger electron-donating capabilities. The blue regions near hydrogen atoms remain consistent but may slightly shift due to changes in molecular geometry and charge distribution [93].

The MEP analysis demonstrates a clear trend in the $[Ace]^-$ series, where reducing the number of ethanol groups from three to one in cations results in more concentrated charge regions. This is visualized through increasingly distinct separation of red (negative) and blue (positive) regions in the MEP surfaces. The last two structures feature $[MEOA]^+$ cations paired with $[Lac]^-$ and $[For]^-$ anions. The maps highlight distinct differences between these anions. $[Lac]^-$ introduces additional functional groups that increase nucleophilicity, as seen by the pronounced red regions around its oxygen atoms. $[For]^-$, on the other hand, has a simpler structure but exhibits concentrated nucleophilic zones due to its high charge density. These variations in MEP distributions significantly influence the compounds' potential applications, particularly in areas requiring specific ionic interactions. The structural characteristics and corresponding MEP distributions of these compounds suggest that the modification of the $[MEOA]^+$ and the choice of anion ($[Ace]^-$ versus $[Lac]^-$) provide a means to tune the electronic properties of these PILs. The systematic variation in charge distribution, particularly evident in the $[Ace]^-$ series, demonstrates how structural modifications can be used to optimize these compounds for specific applications [76,94]. The presence of hydroxyl groups and their number appears to play a significant role in determining the overall ESP distribution, with fewer hydroxyl groups leading to more pronounced charge

separation [95]. This understanding of the relationship between structure and charge distribution is valuable for the rational design of PILs with specific properties, potentially allowing for the development of task-specific PILs optimized for particular applications. These could be the possible reasons for better solubility of guaiacol with [MEOA][Ace], however these do not explain the insolubility of same PILs with syringol.

Understanding the demethylation mechanism in the presence of various anion and cation combinations is both advantageous and essential. In the next step, an implicit solvation model-based calculation was performed to analyze the energy barrier associated with the demethylation of guaiacol in the presence of various anions combined with $[MEOA]^+$. The demethylation of guaiacol in PIL systems offers a fascinating exploration of how various ionic conditions affect reaction pathways while preserving comparable mechanistic characteristics. This section utilizes two unique PIL systems - [MEOA][For](ε=61), and [MEOA][Lac] (ε=58.4) all analyzed through the CPCM implicit solvation method to explore their influence on reaction energetics (Figure 9) [96,97].

In every system, the reaction initiates from a baseline of 0.0 kcal/mol, creating a shared reference point for analysis and comparison. The reaction pathway subsequently advances through a notable energy ascent to generate the initial intermediate, necessitating around 61 kcal/mol in both $[For]^-$ and $[Lac]^-$ systems. The initial energy demand indicates a significant activation barrier that needs to be surpassed to commence the demethylation process. The subsequent transition state exhibits notable consistency across all three ionic environments, albeit with slight variations. The energy profile shows a subtle yet clear barrier separating the first intermediate from the transition state, suggesting a regulated reaction pathway instead of an unprompted change. This regulated advancement is especially noticeable in the $[For]^-$ and $[Lac]^-$ systems, where the energies of the transition states linger around 66 kcal/mol.

After reaching the transition state, all three systems exhibit a steep decline in energy as they progress toward the formation of the second intermediate. This significant decrease in energy indicates a progression that is thermodynamically advantageous once the primary activation barrier is surpassed. The pathways subsequently align towards comparable product energy levels, with the final states exhibiting slightly negative relative energies ranging from -4 to -5 kcal/mol, thereby affirming the overall thermodynamic viability of the demethylation process.

The closely aligned dielectric constants of these PILs (spanning from 58.4 to 61) lead to similar reaction profiles, while each system retains its distinct properties. The $[For]^-$ system, boasting the highest dielectric constant (ε=61), presents the most consistent energy profile. The $[Lac]^-$ system exhibits behavior that is quite similar to that of the $[For]^-$ system, indicating that minor changes in dielectric constant are unlikely to have a substantial impact on the reaction pathway within this range. This detailed examination of the reaction pathways shows that although the overall

mechanism stays the same across various PIL systems, slight differences in the solvent environment can affect the energy requirements of the reaction [98].

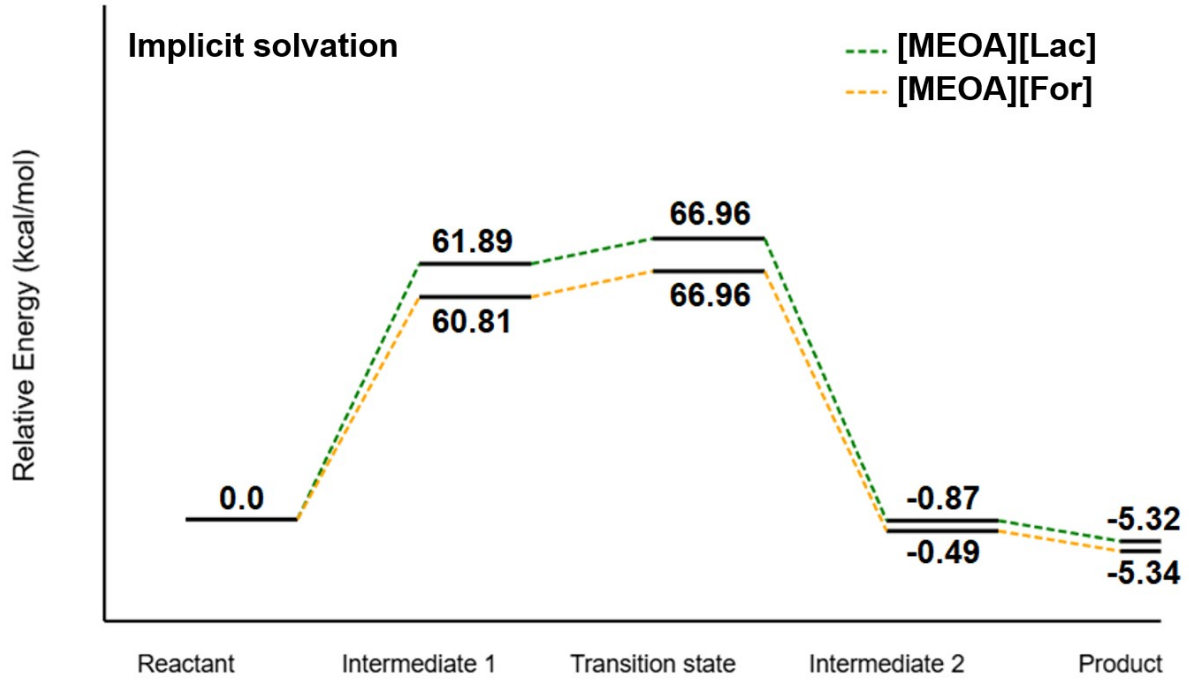

Figure 9. Reaction pathway for demethylation of guaiacol in presence of different PIL systems using CPCM implicit solvation model. The values mentioned with the PIL names in the plots are the dielectric constant of the PILs.

Conclusions

In this work, DFT based calculations were employed to understand the demethylation mechanisms of lignin model compounds (guaiacol and syringol) in PILs. COSMO-RS calculations identified [MEOA][Ace] as the most effective solvent system, demonstrating favorable solubility characteristics, with negative ln(γ) values for guaiacol (-2.5) and slightly positive values for syringol (0.5). Reaction pathway elucidation using implicit and explicit solvation models confirmed an acid-catalyzed hydrolytic mechanism, with guaiacol having a lower activation energy barrier (66.97 kcal/mol) compared to syringol (75.21 kcal/mol), consistent with COSMO-RS predicted solubility data. Furthermore, a systematic decrease in activation energy barriers with increasing acetic acid concentrations in the [MEOA][Ace] PIL system highlighted the potential for kinetic enhancement while maintaining stable product energetics. NCI plots confirm significant steric hindrance in syringol due to its bulky methoxy groups, as indicated by repulsive spikes in the RDG plot, while guaiacol shows negligible steric effects, enabling better solute-solvent integration, improved solubility and lower energy barriers.

Electronic structure calculations revealed a significant reduction in HOMO-LUMO gaps, indicative of increased reactivity for both guaiacol and syringol in PIL environments. The most favorable methyl group charge displacement (+49.47 kJ/mol) was observed in [MEOA][Ace], correlating with its highest positive potential value among all evaluated systems, providing molecular-level validation for its superior demethylation efficiency. These findings offer key insights into the design of PIL-based strategies for targeted C-O bond cleavage in lignin-derived methoxy aromatics.

Looking ahead, the disclosed ability to modulate acid concentrations in PILs to optimize demethylation kinetics could be extended to other acid-driven transformations in biomass valorization. This study will also pave the way for exploring the tunability of PILs for selective bond cleavage in more complex lignin-derived molecules and assessing their viability in experimental settings. Nevertheless, integrating computational and experimental approaches will be critical for advancing PIL-based systems in robust biomass utilization and green chemistry applications.

Competing Interest Statement

BAS has a financial interest in Illium Technologies, Caribou Biofuels, and Erg Bio. None of the other authors have any outside financial interests.

Acknowledgements

The work conducted at the Joint BioEnergy Institute was supported by the U.S. Department of Energy, Office of Science, Biological and Environmental Research Program, through contract DE-AC02-05CH11231 between Lawrence Berkeley National Laboratory and the U.S. Department of Energy. Sandia National Laboratories is a multimission laboratory managed and operated by National Technology & Engineering Solutions of Sandia, LLC, a wholly owned subsidiary of Honeywell International Inc., for the U.S. Department of Energy's National Nuclear Security Administration under contract DE-NA0003525. The United States Government retains and the publisher, by accepting the article for publication, acknowledges that the United States Government retains a nonexclusive, paid-up, irrevocable, worldwide license to publish or reproduce the published form of this manuscript, or allow others to do so, for United States Government purposes. This paper describes objective technical results and analysis. Any subjective views or opinions that might be expressed in the paper do not necessarily represent the views of the U.S. Department of Energy or the United States Government.

References

[1] W. Schutyser, T. Renders, S. Van den Bosch, S. F. Koelewijn, G. T. Beckham, B. F. Sels, *Chem. Soc. Rev.* **2018**, *47*, 852–908.

[2] C. L. Bourmaud, S. Bertella, A. Bosch Rico, S. D. Karlen, J. Ralph, J. S. Luterbacher,

Angew. Chem. Int. Ed **2024**, *63*, e202404442.
[3] J. Ralph, C. Lapierre, W. Boerjan, *Curr. Opin. Biotechnol.* **2019**, *56*, 240–249.
[4] A. J. Ragauskas, G. T. Beckham, M. J. Biddy, R. Chandra, F. Chen, M. F. Davis, B. H. Davison, R. A. Dixon, P. Gilna, M. Keller, P. Langan, A. K. Naskar, J. N. Saddler, T. J. Tschaplinski, G. A. Tuskan, C. E. Wyman, *Science* **2014**, *344*, 1246843.
[5] S. Shrestha, S. Goswami, D. Banerjee, V. Garcia, E. Zhou, C. N. Olmsted, E. L.-W. Majumder, D. Kumar, D. Awasthi, A. Mukhopadhyay, S. W. Singer, J. M. Gladden, B. A. Simmons, H. Choudhary, *ChemSusChem* **2024**, *17*, e202301460.
[6] H. Wang, Y. Pu, A. Ragauskas, B. Yang, *Bioresour. Technol.* **2019**, *271*, 449–461.
[7] A. Beaucamp, M. Muddasar, I. S. Amiinu, M. Moraes Leite, M. Culebras, K. Latha, M. C. Gutiérrez, D. Rodriguez-Padron, F. del Monte, T. Kennedy, K. M. Ryan, R. Luque, M.-M. Titirici, M. N. Collins, *Green Chem.* **2022**, *24*, 8193–8226.
[8] C. Li, X. Zhao, A. Wang, G. W. Huber, T. Zhang, *Chem. Rev.* **2015**, *115*, 11559–11624.
[9] V. Jassal, C. Dou, N. Sun, S. Singh, B. A. Simmons, H. Choudhary, *Front. Chem. Eng.* **2022**, *4*, DOI 10.3389/fceng.2022.1059305.
[10] W. Zhao, C. Wei, Y. Cui, J. Ye, B. He, X. Liu, J. Sun, *Chemical Engineering Journal* **2022**, *443*, 136486.
[11] J.-F. Li, Z.-M. Li, J.-B. Xu, C.-Y. Guo, G.-W. Fang, Y. Zhou, M.-S. Sun, D.-J. Tao, *Ind. Eng. Chem. Res.* **2024**, *63*, 3282–3289.
[12] X. Wu, E. Smet, F. Brandi, D. Raikwar, Z. Zhang, B. U. W. Maes, B. F. Sels, *Angew. Chem. Int. Ed* **2024**, *63*, e202317257.
[13] L. An, C. Si, G. Wang, W. Sui, Z. Tao, *Industrial Crops and Products* **2019**, *128*, 177–185.
[14] S. Zhao, M. M. Abu-Omar, *ACS Sustain. Chem. Eng.* **2017**, *5*, 5059–5066.
[15] X. Zhen, H. Li, Z. Xu, Q. Wang, J. Xu, S. Zhu, Z. Wang, Z. Yuan, *Industrial Crops and Products* **2021**, *173*, 114135.
[16] J. Li, J. Zhang, S. Zhang, Q. Gao, J. Li, W. Zhang, *Polymers (Basel)* **2017**, *9*, DOI 10.3390/polym9090428.
[17] D. Sang, X. Tu, J. Tian, Z. He, M. Yao, *ChemistrySelect* **2018**, *3*, 10103–10107.
[18] K. Sawamura, Y. Tobimatsu, H. Kamitakahara, T. Takano, *ACS Sustain. Chem. Eng.* **2017**, *5*, 5424–5431.
[19] M. E. Wolf, D. J. Hinchen, J. E. McGeehan, L. D. Eltis, *J. Biol. Chem.* **2024**, *300*, 107809.
[20] E. S. Ellis, D. J. Hinchen, A. Bleem, L. Bu, S. J. B. Mallinson, M. D. Allen, B. R. Streit, M. M. Machovina, Q. V. Doolin, W. E. Michener, C. W. Johnson, B. C. Knott, G. T. Beckham, J. E. McGeehan, J. L. DuBois, *JACS Au* **2021**, *1*, 252–261.
[21] S. J. B. Mallinson, M. M. Machovina, R. L. Silveira, M. Garcia-Borràs, N. Gallup, C. W. Johnson, M. D. Allen, M. S. Skaf, M. F. Crowley, E. L. Neidle, K. N. Houk, G. T. Beckham, J. L. DuBois, J. E. McGeehan, *Nat. Commun.* **2018**, *9*, 2487.
[22] L. Zhang, D. Zhao, M. Feng, B. He, X. Chen, L. Wei, S.-R. Zhai, Q.-D. An, J. Sun, *ACS*

Sustain. Chem. Eng. **2019**, *7*, 18593–18602.
[23] B. R. Taylor, N. Kumar, D. K. Mishra, B. A. Simmons, H. Choudhary, K. L. Sale, *Molecules* **2024**, *29*, DOI 10.3390/molecules29215073.
[24] L. T. M. Pham, H. Choudhary, R. Gauttam, S. W. Singer, J. M. Gladden, B. A. Simmons, S. Singh, K. L. Sale, *Front. Energy Res.* **2022**, *10*, DOI 10.3389/fenrg.2022.863153.
[25] D. K. Mishra, G. Gopakumar, G. Pugazhenthi, C. V. Siva Brahmmananda Rao, S. Nagarajan, T. Banerjee, *J. Phys. Chem. A* **2021**, *125*, 9680–9690.
[26] W. Kohn, A. D. Becke, R. G. Parr, *J. Phys. Chem.* **1996**, *100*, 12974–12980.
[27] B. Cao, J. Du, D. Du, H. Sun, X. Zhu, H. Fu, *Carbohydr. Polym.* **2016**, *149*, 348–356.
[28] R. S. Payal, R. Bharath, G. Periyasamy, S. Balasubramanian, *J. Phys. Chem. B* **2012**, *116*, 833–840.
[29] M. Bursch, J.-M. Mewes, A. Hansen, S. Grimme, *Angew. Chem. Int. Ed* **2022**, *61*, e202205735.
[30] H. B. Schlegel, *J. Comput. Chem.* **2003**, *24*, 1514–1527.
[31] D. Glas, C. Van Doorslaer, D. Depuydt, F. Liebner, T. Rosenau, K. Binnemans, D. E. De Vos, *J. Chem. Technol. Biotechnol.* **2015**, *90*, 1821–1826.
[32] A. Casas, J. Palomar, M. V. Alonso, M. Oliet, S. Omar, F. Rodriguez, *Industrial Crops and Products* **2012**, *37*, 155–163.
[33] M. Mohan, K. Huang, V. Pidatala, B. Simmons, S. Singh, K. L. Sale, J. Gladden, *Green Chem.* **2022**, *24*, 1165–1176.
[34] Y. Zhu, Z. Han, L. Fu, C. Liu, D. Zhang, *J. Mol. Model.* **2018**, *24*, 322.
[35] B. G. Janesko, *Phys. Chem. Chem. Phys.* **2011**, *13*, 11393–11401.
[36] B. G. Janesko, *Phys. Chem. Chem. Phys.* **2014**, *16*, 5423–5433.
[37] P. Y. S. Nakasu, P. Verdía Barbará, A. E. J. Firth, J. P. Hallett, *Trends in Chemistry* **2022**, *4*, 175–178.
[38] B. Wang, L. Qin, T. Mu, Z. Xue, G. Gao, *Chem. Rev.* **2017**, *117*, 7113–7131.
[39] P. Verdía Barbará, H. Choudhary, P. S. Nakasu, A. Al-Ghatta, Y. Han, C. Hopson, R. I. Aravena, D. K. Mishra, A. Ovejero-Pérez, B. A. Simmons, J. P. Hallett, *Chem. Rev.* **2025**, DOI 10.1021/acs.chemrev.4c00754.
[40] A. S. Amarasekara, *Chem. Rev.* **2016**, *116*, 6133–6183.
[41] E. M. Morais, I. Abdurrokhman, A. Martinelli, *J. Mol. Liq.* **2022**, *360*, 119358.
[42] T. C. Pin, P. Y. S. Nakasu, S. Mattedi, S. C. Rabelo, A. C. Costa, *Fuel* **2019**, *235*, 1506–1514.
[43] J. F. Leal Silva, P. Y. S. Nakasu, A. C. da Costa, R. Maciel Filho, S. C. Rabelo, *Industrial Crops and Products* **2022**, *189*, 115788.
[44] A. George, A. Brandt, K. Tran, S. M. S. N. S. Zahari, D. Klein-Marcuschamer, N. Sun, N. Sathitsuksanoh, J. Shi, V. Stavila, R. Parthasarathi, S. Singh, B. M. Holmes, T. Welton, B. A. Simmons, J. P. Hallett, *Green Chem.* **2015**, *17*, 1728–1734.

[45] J. Sun, N. V. S. N. M. Konda, R. Parthasarathi, T. Dutta, M. Valiev, F. Xu, B. A. Simmons, S. Singh, *Green Chem.* **2017**, *19*, 3152–3163.
[46] H. Shekaari, M. T. Zafarani-Moattar, S. Faraji, *J. Chem. Eng. Data* **2021**, *66*, 1890–1899.
[47] M. Gődény, C. Schröder, *Liquids* **2025**, *5*, 8.
[48] G. te Velde, F. M. Bickelhaupt, E. J. Baerends, C. Fonseca Guerra, S. J. A. van Gisbergen, J. G. Snijders, T. Ziegler, *J. Comput. Chem.* **2001**, *22*, 931–967.
[49] F. Furche, R. Ahlrichs, C. H?ttig, W. Klopper, M. Sierka, F. Weigend, *WIREs Comput Mol Sci* **2014**, *4*, 91–100.
[50] J. P. Perdew, W. Yue, *Phys. Rev. B* **1986**, *33*, 8800–8802.
[51] J. Zheng, X. Xu, D. G. Truhlar, *Theor. Chem. Acc.* **2011**, *128*, 295–305.
[52] H. Hirao, *J. Phys. Chem. A* **2011**, *115*, 9308–9313.
[53] D. Coskun, S. V. Jerome, R. A. Friesner, *J. Chem. Theory Comput.* **2016**, *12*, 1121–1128.
[54] F. Neese, F. Wennmohs, U. Becker, C. Riplinger, *J. Chem. Phys.* **2020**, *152*, 224108.
[55] J. Tirado-Rives, W. L. Jorgensen, *J. Chem. Theory Comput.* **2008**, *4*, 297–306.
[56] S. Maeda, Y. Harabuchi, Y. Ono, T. Taketsugu, K. Morokuma, *Int. J. Quantum Chem.* **2015**, *115*, 258–269.
[57] T. Lu, *J. Chem. Phys.* **2024**, *161*, DOI 10.1063/5.0216272.
[58] W. Humphrey, A. Dalke, K. Schulten, *J. Mol. Graph.* **1996**, *14*, 33–38, 27.
[59] R. M. Dias, S. M. Vilas-Boas, M. C. da Costa, *Separation and Purification Technology* **2024**, *350*, 127977.
[60] N. D. Austin, N. V. Sahinidis, D. W. Trahan, *Chem. Eng. Sci.* **2017**, *159*, 93–105.
[61] M. Mohan, B. A. Simmons, K. L. Sale, S. Singh, *Sci. Rep.* **2023**, *13*, 271.
[62] D. K. Mishra, B. Banerjee, G. Pugazhenthi, T. Banerjee, *Ind. Eng. Chem. Res.* **2021**, *60*, 9764–9776.
[63] M. Mohan, K. L. Sale, R. S. Kalb, B. A. Simmons, J. M. Gladden, S. Singh, *ACS Sustain. Chem. Eng.* **2022**, DOI 10.1021/acssuschemeng.2c03373.
[64] D. K. Mishra, R. Hussain, G. Pugazhenthi, T. Banerjee, *ACS Sustain. Chem. Eng.* **2022**, *10*, 6157–6164.
[65] J. Gebhardt, M. Kiesel, S. Riniker, N. Hansen, *J. Chem. Inf. Model.* **2020**, *60*, 5319–5330.
[66] I. Abdurrokhman, K. Elamin, O. Danyliv, M. Hasani, J. Swenson, A. Martinelli, *J. Phys. Chem. B* **2019**, *123*, 4044–4054.
[67] N. K. Gupta, P. Reif, P. Palenicek, M. Rose, *ACS Catal.* **2022**, *12*, 10400–10440.
[68] S. Ntakirutimana, T. Xu, H. Liu, J.-Q. Cui, Q.-J. Zong, Z.-H. Liu, B.-Z. Li, Y.-J. Yuan, *Green Chem.* **2022**, *24*, 5460–5478.
[69] M. Aschi, F. Mazza, A. Di Nola, *Journal of Molecular Structure: THEOCHEM* **2002**, *587*, 177–188.
[70] E. Fritschka, G. Sadowski, *Fluid Phase Equilib.* **2024**, *580*, 114039.
[71] I. A. Sedov, T. I. Magsumov, T. M. Salikov, B. N. Solomonov, *Phys. Chem. Chem. Phys.*

2017, *19*, 25352–25359.
[72] R. E. Skyner, J. L. McDonagh, C. R. Groom, T. van Mourik, J. B. O. Mitchell, *Phys. Chem. Chem. Phys.* **2015**, *17*, 6174–6191.
[73] P. Gisdakis, N. Rösch, *European J. Org. Chem.* **2001**, *2001*, 719–723.
[74] J. V. Burda, A. Toro-Labbé, S. Gutiérrez-Oliva, J. S. Murray, P. Politzer, *J. Phys. Chem. A* **2007**, *111*, 2455–2457.
[75] S. Ghosh, S. H. Hassan, A. Das, *J. Phys. Chem. B* **2024**, *128*, 2905–2921.
[76] S. Hafizi Yazdabadi, D. Mihrin, K. L. Feilberg, R. Wugt Larsen, *Molecules* **2024**, *29*, DOI 10.3390/molecules29235521.
[77] J. Bailey, E. L. Byrne, P. Goodrich, P. Kavanagh, M. Swadźba-Kwaśny, *Green Chem.* **2024**, DOI 10.1039/D3GC03297C.
[78] A. J. Eugene, E. A. Pillar-Little, A. J. Colussi, M. I. Guzman, *Langmuir* **2018**, *34*, 9307–9313.
[79] M. G. Freire, C. M. S. S. Neves, I. M. Marrucho, J. A. P. Coutinho, A. M. Fernandes, *J. Phys. Chem. A* **2010**, *114*, 3744–3749.
[80] M. A. Morsali, H. Shekaari, B. Golmohammadi, *Sci. Rep.* **2024**, *14*, 27229.
[81] A. R. Abouelela, P. Y. S. Nakasu, J. P. Hallett, *ACS Sustain. Chem. Eng.* **2023**, *11*, 2404–2415.
[82] N. I. Haykir, *Journal of Wood Chemistry and Technology* **2022**, *42*, 91–103.
[83] A. McGrogan, E. L. Byrne, R. Guiney, T. F. Headen, T. G. A. Youngs, A. Chrobok, J. D. Holbrey, M. Swadźba-Kwaśny, *Phys. Chem. Chem. Phys.* **2023**, *25*, 9785–9795.
[84] N. K. Das, D. K. Mishra, P. K. Naik, P. Dehury, S. Bose, T. Banerjee, *Journal of Energy Storage* **2023**, *59*, 106365.
[85] J. Aihara, *J. Phys. Chem. A* **1999**, *103*, 7487–7495.
[86] S.-Y. Chu, *Tetrahedron* **1978**, *34*, 645–647.
[87] J. L. Bregado, A. R. Secchi, F. W. Tavares, *Phys. Chem. Chem. Phys.* **2024**, *26*, 9234–9252.
[88] S.-Y. Chu, *Chem. Phys. Lett.* **1977**, *46*, 505–508.
[89] M. Franco-Pérez, J. L. Gázquez, *J. Phys. Chem. A* **2019**, *123*, 10065–10071.
[90] A. Conde, R. Fandos, C. Hernández, A. Otero, A. Rodríguez, M. J. Ruiz, *Chem. Eur. J* **2012**, *18*, 2319–2326.
[91] J. Zhang, T. Lu, *Phys. Chem. Chem. Phys.* **2021**, *23*, 20323–20328.
[92] T. Lu, S. Manzetti, *Struct. Chem.* **2014**, *25*, 1521–1533.
[93] S. Manzetti, T. Lu, *J. Phys. Org. Chem.* **2013**, *26*, 473–483.
[94] H. Ji, P. Lv, *Green Chem.* **2020**, *22*, 1378–1387.
[95] Y. Sun, X. Jia, R. Yang, X. Qin, X. Zhou, H. Zhang, W. Kong, J. Zhang, J. Wang, *Carbohydr. Polym.* **2022**, *284*, 119159.
[96] M. Stahn, S. Ehlert, S. Grimme, *J. Phys. Chem. A* **2023**, *127*, 7036–7043.

[97] Y. Takano, K. N. Houk, *J. Chem. Theory Comput.* **2005**, *1*, 70–77.
[98] J. Zhang, H. Zhang, T. Wu, Q. Wang, D. van der Spoel, *J. Chem. Theory Comput.* **2017**, *13*, 1034–1043.